

Efficient Adsorption of Azo Dye Acid Brilliant Red on Graphite Carbon Nitride in Aqueous Solution

Huiwen Sun and Yongjun Liu*



Cite This: *ACS Omega* 2024, 9, 28626–28636



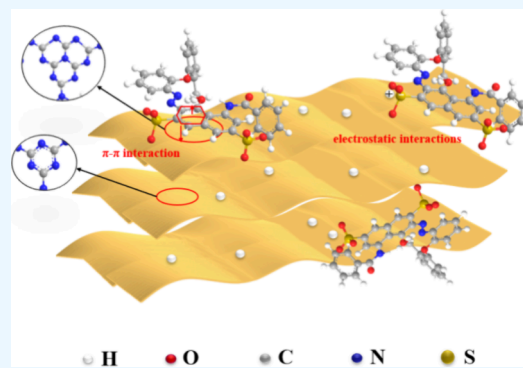
Read Online

ACCESS |

Metrics & More

Article Recommendations

ABSTRACT: In this study, two types of graphite carbon nitrides were prepared by directly calcinating urea (U- $g\text{-C}_3\text{N}_4$) and melamine (M- $g\text{-C}_3\text{N}_4$) in a muffle furnace. Their adsorption performances on acid brilliant red (ABR) from aqueous solution were examined and compared. Results showed that, at the optimum calcination temperature of 580 °C, both the adsorption capacity of U- $g\text{-C}_3\text{N}_4$ and that of M- $g\text{-C}_3\text{N}_4$ increased strongly with decreasing solution pH. U- $g\text{-C}_3\text{N}_4$ exhibits higher adsorption capacity than M- $g\text{-C}_3\text{N}_4$ at an initial pH > 2.0. However, at an initial pH of 1.0, M- $g\text{-C}_3\text{N}_4$ displayed a much higher adsorption capacity than U- $g\text{-C}_3\text{N}_4$, where the maximum adsorption capacity of M- $g\text{-C}_3\text{N}_4$ can reach 25 635.64 mg g⁻¹, being the highest reported to date. Adsorptions of both adsorbents followed pseudo-second-order kinetic models and the Langmuir adsorption isothermal models. The adsorption is spontaneous and exothermic and occurs mainly through electrostatic attraction between the protonated $g\text{-C}_3\text{N}_4$ and the negatively charged ABR. In addition, the used U- $g\text{-C}_3\text{N}_4$ can be easily regenerated with ethanol and the renewed U- $g\text{-C}_3\text{N}_4$ possesses comparable adsorption capability of its original form, showing its superior recyclability and broad industrial application prospects.



1. INTRODUCTION

Dyeing and printing processes in the textile industry have seriously contributed to the pollution of water bodies. Acid dyes, often containing azo groups, constitute the largest portion of the artificial dyes. These dyes are discharged into the environment in the form of wastewater, resulting in considerable deterioration of the receiving water quality.¹ Wastewater contaminated with acid dyes is characterized by high chromaticity, poor biodegradability, and high concentration.^{2,3} Removal of acid dyes from wastewater is becoming a challenge due to the antioxidation design and increasingly stringent discharge standards.

Acid dyes in wastewater can be removed via photocatalytic decomposition, chemical reduction, biological oxidation, etc.⁴ Photocatalytic decomposition is usually energy-consuming and process complexing if an artificial light source is used.^{5,6} Chemical reduction uses chemical reductants to destroy the azo bond and results in a lot of toxic byproducts.⁷ Biological oxidation is cost-effective; however, the long operation time and the requirement of strict operating conditions limit its application in real dye wastewater treatment.⁸

Adsorption^{9–11} is an effective and environmentally friendly method that has been applied in many dye wastewater treatments. Activated carbon (AC) is the most utilized adsorbent for the removal of dyes from water.⁹ However, the adsorption capacity of AC is low, and the recyclability is poor.

Development of highly efficient and reusable adsorbents is urgently desirable.^{12–14}

At present, graphite carbon nitride ($g\text{-C}_3\text{N}_4$) is being extensively studied in the photocatalytic decomposition of aqueous organic pollutants^{15,16} since Wang et al. reported that it can split water into H₂ under visible light irradiation.¹⁷ $g\text{-C}_3\text{N}_4$ is a stable and nonmetallic semiconductor with a band gap of 2.7 eV, which means that it can utilize solar energy to drive the photocatalytic reactions in aqueous solution. Tremendous work has been reported in terms of organic pollutant degradation.¹⁵ It shows that $g\text{-C}_3\text{N}_4$ also adsorbs the target pollutants during the degradation.¹⁸ Zhu et al.¹⁹ studied the isoelectric point and found that methylene blue was moderately adsorbed and methyl orange was hardly adsorbed by $g\text{-C}_3\text{N}_4$. Stefa et al.²⁰ revealed that $g\text{-C}_3\text{N}_4$ nanosheets exhibit no adsorption on anionic ones. As $g\text{-C}_3\text{N}_4$ is rich in nitrogen-containing groups, it can offer lone pair electrons to form complexes with metallic cations or salts with acids. $g\text{-C}_3\text{N}_4$ has been shown to adsorb heavy metal ions in an

Received: March 20, 2024

Revised: May 29, 2024

Accepted: June 7, 2024

Published: June 20, 2024



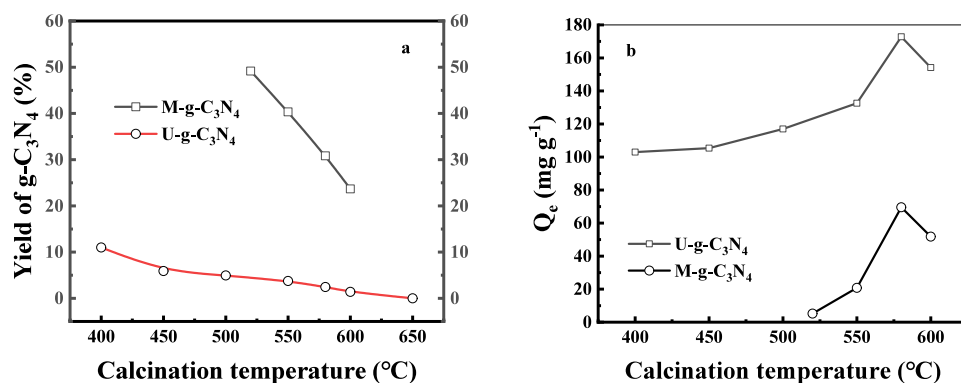


Figure 1. Dependences of yield (a) and adsorption capacity (b) of U-g-C₃N₄ and M-g-C₃N₄ on calcination temperature (adsorbent dose, 100 mg; initial ABR concentration, 100 mg L⁻¹; initial pH of ABR solution, 3.0; solution volume, 200 mL; adsorption temperature, 298.15 K).

aqueous solution. g-C₃N₄ possesses a highly ordered tris-triazine (C₆N₇) unit, which should adsorb organic dyes via hydrophobic effects and π - π interactions.²¹ On the other hand, hydrogen bonding also plays an important role in the adsorption.²² Selective adsorption of humic acids from landfill leachate can also be achieved.²³ In contrast to photocatalysis, using g-C₃N₄ for removing acid dyes occurs quite little.^{24–26}

In this study, g-C₃N₄ was prepared using urea (U-g-C₃N₄) and melamine (M-g-C₃N₄) as precursors. In addition, their respective adsorption properties on acid brilliant red (ABR) were evaluated and compared in detail. ABR is a typical acid dye, widely applied in coloring silk, wool, polyamides, and acrylic fibers.²⁷ Chitosan,¹² modified nanomaterials,¹³ and AC¹⁴ have been employed for removal of ABR from water. Effects of some important parameters on adsorption were also examined. Adsorption kinetic and thermodynamic analyses were also performed to elucidate possible adsorption mechanisms. In addition, reusability experiments were conducted.

2. MATERIALS AND METHODS

2.1. Materials. Melamine [C₃N₃(NH₂)₃] and urea [(NH₂)₂CO] were purchased from Kermel Chemical Reagent Company (Tianjin, China). ABR was obtained from Wu Jiang Tong Luo Dyestuff Chemical Company (Jiangsu, China). Reagents mentioned above were of analytical reagent grade, without further purification. Hydrochloric acid [HCl] and sodium hydroxide [NaOH] were purchased from HoWei Pharmaceutical Company (Guangzhou, China). Distilled water was used throughout all of the experiments.

2.2. Synthesis of U-g-C₃N₄ and M-g-C₃N₄. U-g-C₃N₄ and M-g-C₃N₄ were prepared by directly heating urea and melamine in a muffle furnace, respectively.²⁸ Namely, 18.0 g of urea was heated at 400–650 °C for 2 h, and the heating rate was set to 5 °C/min. The obtained powder was termed U-g-C₃N₄. M-g-C₃N₄ is prepared by calcining melamine: 6.0 g of melamine was heated at 520–600 °C with a heating rate of 5 °C/min for 2 h. The yielded products were grounded into powder; And the powder was then heated at 520–600 °C with a heating rate of 5 °C/min for 1 h.

2.3. ABR Adsorption Experiments. A 100 mg portion of g-C₃N₄ was dispersed in 200 mL of ABR solution stirred at different temperatures (298.15–318.15 K) and different initial pH values (1.0–12.0) with a certain initial ABR concentration of 75–700 mg L⁻¹. During the adsorption, 2.0 mL of the suspension was withdrawn and centrifuged for subsequent

analysis. The concentration of ABR was determined using a UV–vis spectrometer (UV-2600, Shimadzu) by measuring the absorbance of the centrifuged solutions at 492 nm. The adsorption amount (Q_t (mg g⁻¹)) of ABR was determined using eq 1:

$$Q_t = \frac{(C_0 - C_t)V}{m} \quad (1)$$

where V is the volume of ABR solution (L), C_0 and C_t are the initial concentration of ABR and the concentration of ABR at adsorption time t (mg L⁻¹), and m is the mass of g-C₃N₄ (g). It should be noted that the adsorption capacity (Q_e) is obtained from eq 1 when the adsorption gets to equilibrium. The solid separated from the centrifugation was washed with deionized water and dried for the structural analyses.

2.4. Characterizations. Crystallographic structures of the calcined samples were analyzed using X-ray diffraction (XRD, D/max-Ultima+, Rigaku; Bruker D2 Phaser, Cu K α , = 1.5406 Å, 30 kV and 10 mA). Morphologies of the samples were observed by scanning electron microscopy (SEM, SUPRASS). N₂ adsorption–desorption isotherms were conducted on an ASAP2420 surface area analyzer at 77 K. Before the measurements, the samples were degassed at 200 °C for 6 h. Brunauer–Emmett–Teller (BET, TriStar II3030) specific surface areas were determined using the desorption data. Pore size distribution was determined using the Barrett–Joyner–Halenda (BJH) method. X-ray photoelectron spectroscopy (XPS) was conducted on a Thermo Scientific K-AlphaTM+ spectrometer equipped with a monochromatic Al K α X-ray source (1486.6 eV) operating at 100 W. Samples were analyzed under a vacuum ($P < 10^{-8}$ mbar) with a pass energy of 150 eV (survey scans) or 50 eV (high-resolution scans). All peaks were calibrated with a C 1s peak binding energy at 284.8 eV for adventitious carbon. Fourier transformed infrared (FT-IR) spectra were recorded on an FT-IR spectrometer (Nicolet iS Thermo) using a standard KBr pellet technique.

3. RESULTS AND DISCUSSION

3.1. Effect of Calcination Temperature on the Yield and Adsorption Performances. The effect of calcination temperature on the yield and the adsorption capacity (Q_e) of U-g-C₃N₄ or M-g-C₃N₄ are shown in Figure 1.

It can be illustrated from Figure 1a that both the yield of U-g-C₃N₄ and that of M-g-C₃N₄ decrease with an increase in calcination temperature. In addition, the yield of M-g-C₃N₄ is

higher than that of U-g-C₃N₄ at an identical calcination temperature. At 500 °C, the yield of M-g-C₃N₄ is ca. 50% while that of U-g-C₃N₄ is only 5%, meaning that urea releases more gases (e.g., CO₂ and NH₃)²⁸ than melamine during the calcination, which may endow U-g-C₃N₄ with many more pores than M-g-C₃N₄, as evidenced by the following BET analysis.

As shown in Figure 1b, the adsorption of ABR by U-g-C₃N₄ and M-g-C₃N₄ exhibit a similar trend: the adsorption capacity peaks at 580 °C, where it is 172.8 mg g⁻¹ for U-g-C₃N₄ and 69.6 mg g⁻¹ for M-g-C₃N₄. Therefore, the g-C₃N₄'s prepared at 580 °C (M-g-C₃N₄-580 and U-g-C₃N₄-580) were employed as adsorbents in the subsequent investigations.

3.2. Structural Characterizations. SEM images of U-g-C₃N₄-580 and M-g-C₃N₄-580 are presented in Figure 2. It can

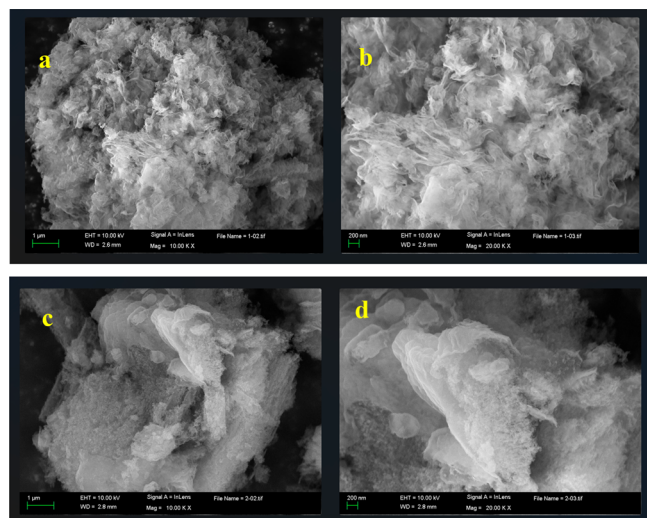


Figure 2. SEM images of U-g-C₃N₄-580 (a,b) and M-g-C₃N₄-580 (c,d).

be shown that U-g-C₃N₄-580 has an observable lamellar folded structure consisting of small flakes with thicknesses of approximately 10 nm, which may provide numerous adsorption sites for the adsorption of dyes.²⁶ M-g-C₃N₄-580 exhibited a similar structure to that of U-g-C₃N₄-580. It is a blocky structure formed by dense lamellar overlapping, with a smooth surface²⁹ that indicates that the planar surface possesses abundant nitrogen sites.³⁰

Figure 3a and b show the XRD patterns and FT-IR spectra of U-g-C₃N₄-580 and M-g-C₃N₄-580, respectively. As shown in Figure 3a, two obvious diffraction peaks can be observed in the two samples. The weak peak at 12.9° is related to the repeated units (tri-s-triazine) of the in-plane structure and corresponds to the (100) lattice plane. Another strong diffraction peak, (002), centered at 27.6°, corresponds to the conjugated aromatic system stacking plane.³¹ The diffraction peaks of M-g-C₃N₄-580 were much stronger than those of U-g-C₃N₄-580, suggesting that the crystallite size of M-g-C₃N₄-580 is larger than that of U-g-C₃N₄-580.

As shown in Figure 3b, broad peaks at 3000–3289 cm⁻¹ correspond to the stretching vibrations of the N–H bond in the primary (–NH₂) and secondary (=NH) amine groups, suggesting that the precursor was not fully condensed during the calcination. Peaks at 1639 cm⁻¹, 1573 cm⁻¹, 1464 cm⁻¹, and 1410 cm⁻¹ were assigned to the stretching vibrations of tri-s-triazine repeating units while peaks at 1323 cm⁻¹ and 1245 cm⁻¹ were attributed to the out-of-plane bending vibrations of the tri-s-triazine.³² The sharp peak at 809 cm⁻¹ represents the vibration of the triazine units. The FT-IR spectra results clearly indicated that M-g-C₃N₄-580 possesses more tri-s-triazine units than U-g-C₃N₄-580 and that U-g-C₃N₄-580 contains more triazine rings than M-g-C₃N₄-580. Such a difference may result in different interactions with ARB.³²

Wide scan and C 1s and N 1s high resolution XPS spectra of U-g-C₃N₄-580 and M-g-C₃N₄-580 were presented in Figure 4. Figure 4a shows that M-g-C₃N₄-580 is mainly composed of carbon and nitrogen as well as a small amount of oxygen, while U-g-C₃N₄-580 comprises only carbon and nitrogen. The weak O 1s peak may be originated from oxygen species, such as H₂O and OH, adsorbed on the surface.³³ The high-resolution C 1s spectra consist of three peaks at binding energies of 284.8, 286.8, and 288.3 eV, assigned to the surface adventitious carbon or defect-containing sp² hybridized carbon atoms,¹⁶ C–N=C bonding in the aromatic ring of g-C₃N₄ units,³⁴ and the sp³ hybridized C–N bonding, respectively.²⁴ The high-resolution N 1s spectra can be deconvoluted into three peaks at binding energies of 398.8, 400.6, and 401.5 eV, corresponding to the pyridinic-like N, pyrrolic-like N, and graphitic-like N, respectively.^{35–37}

Figure 5a and b shows the N₂ adsorption–desorption isotherms of U-g-C₃N₄-580 and M-g-C₃N₄-580, respectively. The insets give the corresponding pore size distribution curves obtained from adsorption branch of the isotherms with the Barrett–Joyner–Halenda (BJH) method. As shown in Figure

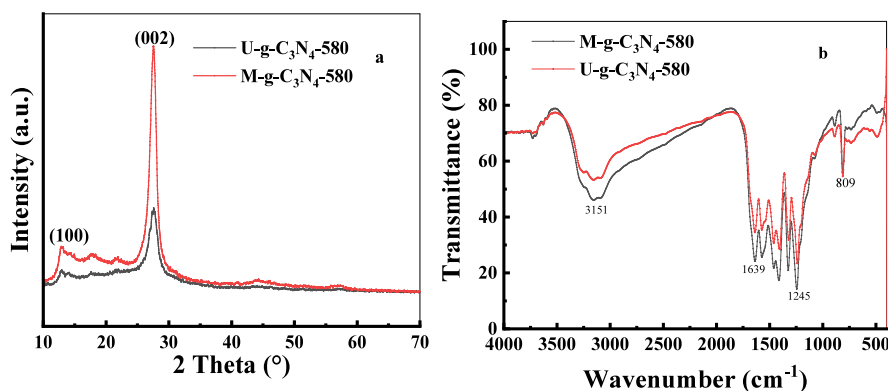


Figure 3. XRD pattern (a) and FT-IR spectra (b) of U-C₃N₄-580 and M-C₃N₄-580.

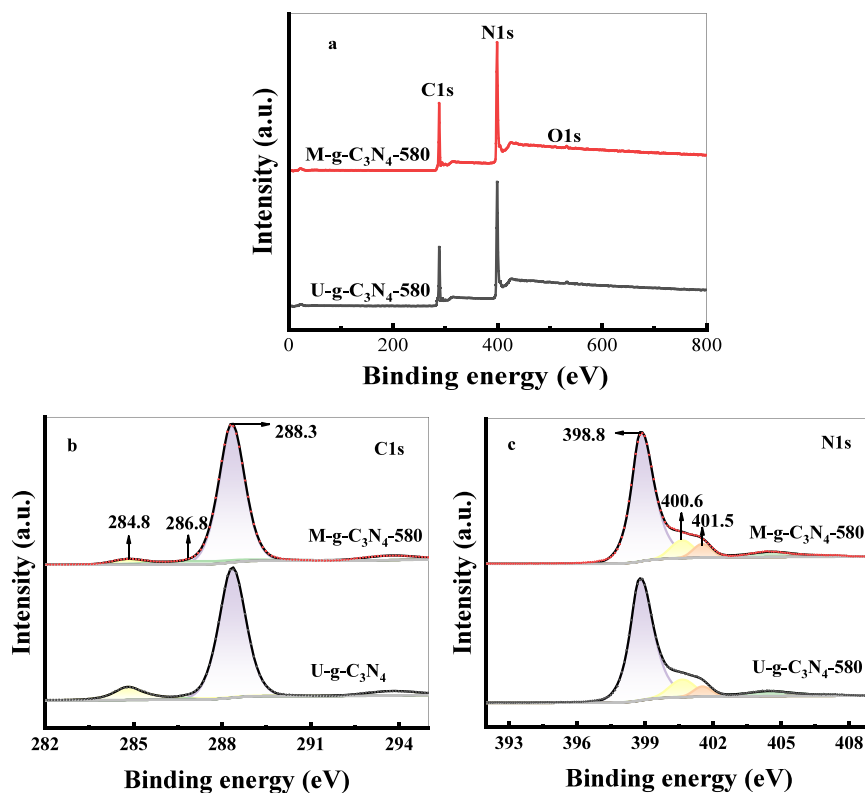


Figure 4. Wide scan XPS spectra (a) and C 1s (b) and N 1s (c) high resolution XPS spectra of U-g-C₃N₄-580 and M-g-C₃N₄-580.

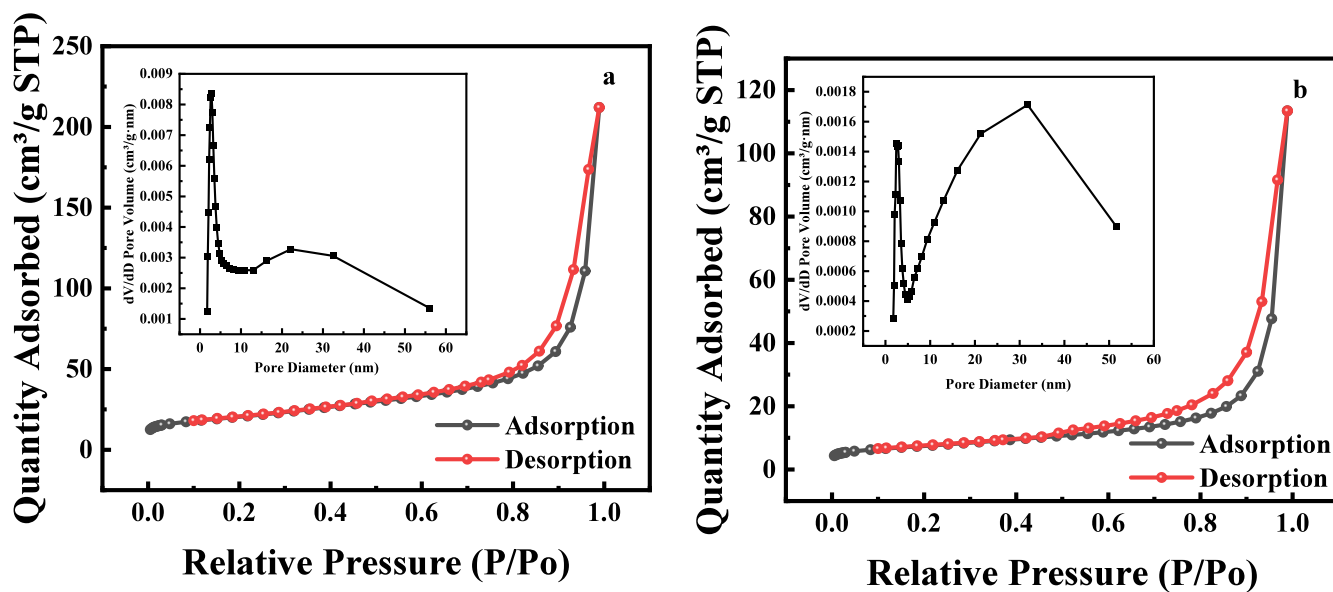


Figure 5. N₂ adsorption–desorption isotherm and pore size distribution curves (inset) of (a) U-g-C₃N₄-580 and (b) M-g-C₃N₄-580.

5a and b, all samples exhibit type IV isotherms with H₃-type hysteresis, at a relative pressure range of 0.6–1.0, implying the possible existence of flake-like pores. The pore size distribution curves reveal that the samples mainly contain flake-like pores centered around 2–5 nm, which means that the samples are mesoporous materials.³⁸

The specific surface area (SSA), pore volume (V_{pore}), and pore size (D_{pore}) of U-g-C₃N₄-580 and M-g-C₃N₄-580 are listed in Table 1. The calculated Brunauer–Emmett–Taylor (BET) specific surface areas of U-C₃N₄-580 and M-C₃N₄-580 were 72.07 and 26.31 m² g⁻¹, respectively. The results indicated that

Table 1. Specific Surface Area, Pore Volume, and Pore Size of U-g-C₃N₄-580 and M-g-C₃N₄-580

| sample | U-g-C ₃ N ₄ -580 | M-g-C ₃ N ₄ -580 |
|--|--|--|
| SSA (m ² /g) | 72.0686 | 26.3141 |
| V_{pore} (cm ³ /g) | 0.329988 | 0.175860 |
| D_{pore} (nm) | 12.3262 | 16.8137 |

the use of urea as the precursor could increase the specific surface area of g-C₃N₄ by 2.74 times.

3.3. Adsorption on ABR. Variations in the value of Q_t with adsorption time were demonstrated in Figure 6. It can be

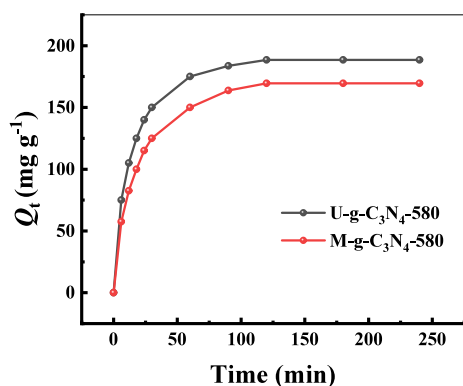


Figure 6. Adsorption of ABR on U- $g-C_3N_4-580$ and M- $g-C_3N_4-580$ with adsorption time (adsorbent dose, 100 mg; initial ABR concentration, 150 $mg\ L^{-1}$; initial pH of ABR solution, 2.0; solution volume, 200 mL; and adsorption temperature, 298.15 K).

manifested that the value of Q_t increases steeply with increasing adsorption time in the first hour, and then a plateau was reached, suggesting that ABR was adsorbed onto $g-C_3N_4-580$ as a monolayer, rather than as multiple layers. In addition, Q_t increased little in an adsorption time longer than 2 h. Therefore, 2 h can be regarded as the equilibrium time in practice. U- $g-C_3N_4-580$ has a higher adsorption capability than M- $g-C_3N_4-580$ under the same experimental conditions. Therefore, most of the next experiments used U- $g-C_3N_4-580$ as the research target.

In order to better describe the adsorption, two kinetic models were attempted to fit the experimental data to describe the adsorption kinetics. The pseudo-first-order model³³ was

$$\ln(Q_e - Q_t) = \ln Q_e - k_1 t \quad (2)$$

and the pseudo-second-order kinetic model³⁹ was

$$\frac{t}{Q_t} = \frac{1}{k_2 Q_e^2} + \frac{t}{Q_e} \quad (3)$$

where the amounts of ABR adsorbed at equilibrium and at time t (min) are represented by Q_e and Q_t ($mg\ g^{-1}$), respectively; k_1 (min^{-1}) and k_2 ($g\ mg^{-1}\ min^{-1}$) stand for the rate constants of pseudo-first order and pseudo-second-order

adsorption, respectively. The linear plots of $\ln(Q_e - Q_t)$ versus t and (t/Q_t) versus t were drawn for the pseudo-first-order and the pseudo-second-order models, respectively, where the rate constants k_1 and k_2 can be derived. The fitting results are given in Figure 7, and the corresponding kinetic parameters and correlation coefficients are listed in Table 2.

Table 2 demonstrates that the correlation coefficient of the pseudo-second-order kinetic model (0.99) is higher than that of the pseudo-first-order kinetic model. Therefore, the adsorption of $g-C_3N_4-580$ on ABR is more consistent with the pseudo-second-order kinetics. In addition, the values of Q_e calculated from the pseudo-second-order kinetic model for U- $g-C_3N_4-580$ and M- $g-C_3N_4-580$ were 198.02 and 181.16 $mg\ g^{-1}$, closer to the actual adsorption capacity. The adsorption kinetic constant for U- $g-C_3N_4-580$ is higher than that for M- $g-C_3N_4-580$, which shows a more favorable interaction between ABR and U- $g-C_3N_4-580$.^{39,40}

3.4. Effect of Initial pH Value on the Adsorption. pH usually plays an important role in the adsorption. In this study, the adsorption was carried out on ABR solutions at initial pH from 1.0 to 12.0, and the results are illustrated in Figure 8.

As indicated in Figure 8, the adsorption capacity (Q_e) of both U- $g-C_3N_4-580$ and M- $g-C_3N_4-580$ increased markedly with a decreasing initial pH value. U- $g-C_3N_4-580$ showed superior adsorption performance to that of M- $g-C_3N_4-580$ when the initial pH value was larger than 2.0. However, the Q_e of M- $g-C_3N_4-580$ is almost equal to that of U- $g-C_3N_4-580$ at initial pH 1.0. It should be noted that both the adsorption ratios reached over 99% in conducting the experiments at an initial pH of 1.0, and this may lead to errors in determinations. Therefore, adsorption experiments of both materials at pH 1.0 with lower adsorbent dosages were further investigated in Figures 9–11.

In acidic solution, ABR was in the anionic form $R-SO_3^-$ and $g-C_3N_4$ was positively charged.²⁹ As a result, an acidic medium is favorable for the adsorption because of the electrostatic attractions between $R-SO_3^-$ and protonated $g-C_3N_4$. However, as observed in Figure 7, under alkaline conditions even at pH 12.0, where almost no protonated $g-C_3N_4$ exists, the adsorption capacity is still above 100 $mg\ g^{-1}$, indicating that interactions other than the electrostatic one between ABR and $g-C_3N_4$ must be present, such as hydrogen bonding and $\pi-\pi$ interactions.^{41,42}

Information on the surface properties, adsorbate affinity, and adsorption capacity of an adsorbent can be obtained from an

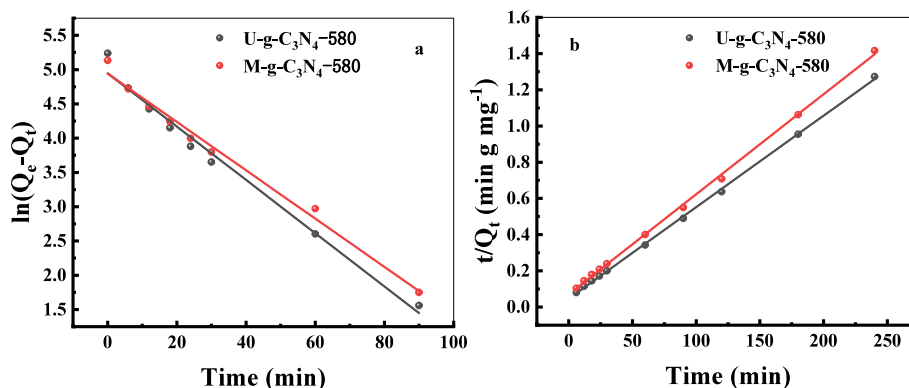


Figure 7. Plots of the pseudo-first-order (a) and pseudo-second-order kinetic models (b) for ABR adsorption on U- $g-C_3N_4-580$ and M- $g-C_3N_4-580$ (data from Figure 6).

Table 2. Adsorption Kinetic Parameters of ABR over U-*g*-C₃N₄-580 and M-*g*-C₃N₄-580

| sample | pseudo-first-order model | | | pseudo-second-order model | | |
|---|--------------------------|----------------------------|-----------------------------|---------------------------|---|-----------------------------|
| | parameters | k_1 (min ⁻¹) | Q_e (mg g ⁻¹) | R^2 | k_2 (g mg ⁻¹ min ⁻¹) | Q_e (mg g ⁻¹) |
| U- <i>g</i> -C ₃ N ₄ -580 | 0.04 | 140.66 | 0.98 | 5.49×10^{-5} | 198.02 | 0.99 |
| M- <i>g</i> -C ₃ N ₄ -580 | 0.03 | 139.99 | 0.98 | 4.31×10^{-5} | 181.16 | 0.99 |

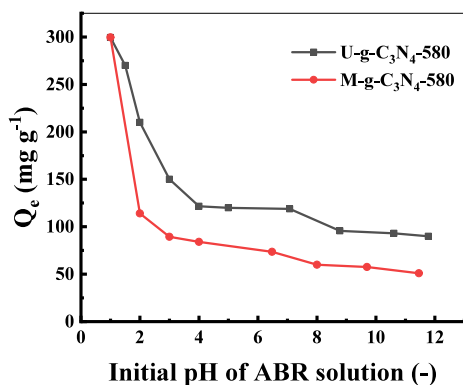


Figure 8. Effect of initial pH of ABR solution on its adsorption on U-*g*-C₃N₄-580 and M-*g*-C₃N₄-580 (adsorbent dose, 100 mg; initial ABR concentration, 150 mg L⁻¹; solution volume, 200 mL; adsorption temperature, 298.15 K).

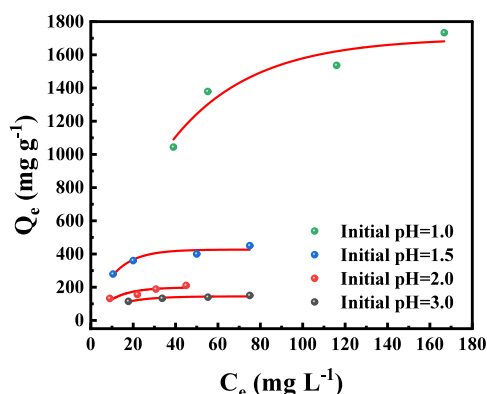


Figure 9. Adsorption isotherms of ABR on U-*g*-C₃N₄-580 at different initial pH values (solution volume, 200 mL; adsorption temperature, 298.15 K; adsorbent dose, 50 mg for initial ABR solution pH 1.0 and 100 mg for initial pH of ABR solution 1.5, 2.0, and 3.0).

adsorption isotherm. The Langmuir and Freundlich isotherm models are two extensively used mathematical models. The Langmuir model assumes a monolayer coverage and that all of the adsorbent sorption sites are the same. The Freundlich isotherm model assumes that the coverage is multilayer and that all of the adsorption sites are heterogeneous⁴³ as follows:

$$\frac{C_e}{Q_e} = \frac{1}{Q_m K_L} + \frac{C_e}{Q_m} \quad (4)$$

$$\ln Q_e = \frac{1}{n} \ln C_e + \ln K_F \quad (5)$$

where Q_e and Q_m (mg g⁻¹) are the adsorption capacity and the maximum adsorption capacity (corresponding to complete monolayer coverage), respectively; C_e (mg L⁻¹) represents the adsorbate concentration at adsorption equilibrium; n is the Freundlich constant; K_L and K_F are the constants corresponding to the energy of sorption (L mg⁻¹) and adsorption performance (mg g⁻¹ (L mg⁻¹)^{1/n}), respectively. Q_m and K_L can be calculated according to the slope and intercept of the linear plot of C_e/Q_e against C_e . n and K_F can be calculated from the slope and intercept of the linear plot of $\ln Q_e$ versus $\ln C_e$.

Adsorption isotherms of U-*g*-C₃N₄-580 at initial pH's of 1.0, 1.5, 2.0, and 3.0 were performed, and the results are shown in Figure 9. It can be observed from Figure 9 that the adsorption capacity of U-*g*-C₃N₄-580 increases with increasing C_e at each initial pH value. These curves are typical type L₁ isotherms, implying high affinity between adsorption sites of U-*g*-C₃N₄-580 and ABR.⁴⁴ U-*g*-C₃N₄-580 has the highest adsorption capacity at the initial pH of 1.0. Fittings of adsorption isothermal curves of Figure 9 are displayed in Figure 10.

As shown in Figure 10a, the Langmuir fitted adsorption isothermal curves showed a gradual increase in the slope and a gradual decrease in the fitted Q_m as the initial pH increased. Parameters calculated from the linear forms of the two isotherms are summarized in Table 3.

The Q_m values fitted at initial pH's of 1.0, 1.5, 2.0, and 3.0 were 2063.04 mg g⁻¹, 490.20 mg g⁻¹, 252.53 mg g⁻¹, and 164.20 mg g⁻¹, respectively. The pH of the solution also affects

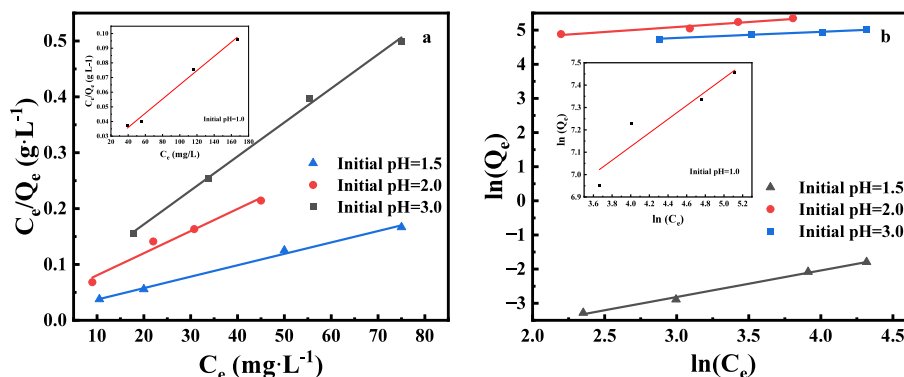


Figure 10. Adsorption isotherms of ABR on U-*g*-C₃N₄-580 fitted with Langmuir (a) and Freundlich (b) models at the initial pH values of 1.0 (inset), 1.5, 2.0, and 3.0 (adsorbent dose, 100 mg; solution volume, 200 mL; adsorption temperature, 298.15 K).

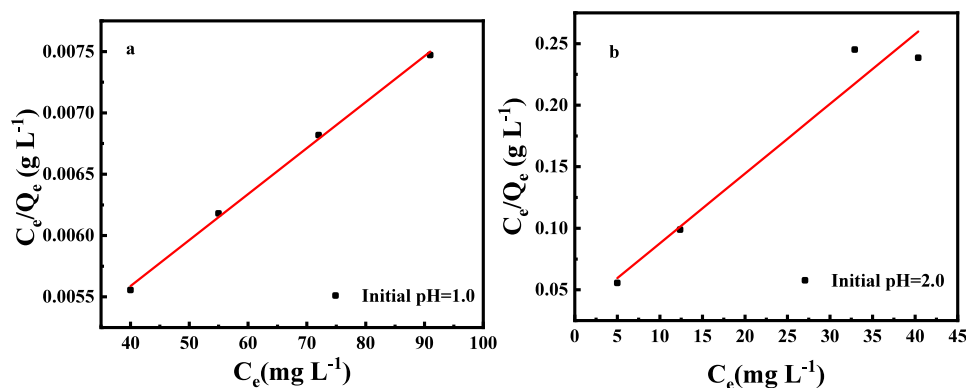


Figure 11. Adsorption isotherm of ABR on M-g-C₃N₄-580 fitted with Langmuir at initial pH 1.0 (a; adsorbent dose, 10 mg; solution volume, 200 mL; temperature, 298.15K) and pH 2.0 (b; adsorbent dose, 100 mg; solution volume, 200 mL; adsorption temperature, 298.15 K).

Table 3. Langmuir and Freundlich Constants for the Adsorption of ABR over U-g-C₃N₄-580 at Different Initial pH Values

| initial pH | Langmuir adsorption isotherm | | | Freundlich adsorption isotherm | | |
|------------|--------------------------------------|--------------------------------------|----------------|--------------------------------|-------------------------------------|----------------|
| | Q _m (mg g ⁻¹) | K _L (L mg ⁻¹) | R ² | n | K _F (L g ⁻¹) | R ² |
| 1.0 | 2063.04 | 0.03 | 0.99 | 3.27 | 365.56 | 0.99 |
| 1.5 | 490.20 | 0.12 | 0.99 | 5.57 | 68.88 | 0.95 |
| 2.0 | 252.53 | 0.10 | 0.99 | 3.43 | 67.87 | 0.98 |
| 3.0 | 164.20 | 0.12 | 0.99 | 1.29 | 0.01 | 0.89 |

the degree of the protonation U-g-C₃N₄-580, usually increased with decreasing pH, thus attracting more ABR molecules.⁴⁵ The Langmuir adsorption model has a stronger correlation and a better fit compared to the fitting of Freundlich adsorption isothermal curves, as shown by the values of R² in Table 3.

Figure 11 shows Langmuir isothermal models of M-g-C₃N₄-580 at initial pH's of 1.0 and 2.0, where the Langmuir constants for the adsorptions are summarized in Table 4.

Table 4. Langmuir Constants for Adsorption of ABR by U-g-C₃N₄-580 and M-g-C₃N₄-580 at Initial pH's of 1.0 and 2.0 (Conditions from Figures 10 and 11)

| initial pH | sample | Q _m (mg g ⁻¹) | K _L (L mg ⁻¹) | R ² |
|------------|--|--------------------------------------|--------------------------------------|----------------|
| 1.0 | U-g-C ₃ N ₄ -580 | 2063.04 | 0.03 | 0.99 |
| | M-g-C ₃ N ₄ -580 | 25635.64 | 0.01 | 0.99 |
| 2.0 | U-g-C ₃ N ₄ -580 | 252.53 | 0.10 | 0.99 |
| | M-g-C ₃ N ₄ -580 | 176.68 | 0.18 | 0.96 |

At an initial pH of 2.0, the Q_m of M-g-C₃N₄-580 was 176.68 mg g⁻¹, less than that of U-g-C₃N₄-580, 252.53 mg g⁻¹, which has the same trend of the results shown in Figure 6. But at the initial pH of 1.0, the Q_m value of M-g-C₃N₄-580 reached 25635.64 mg g⁻¹, being 12.4-fold greater than that of U-g-C₃N₄-580 2063.04 mg g⁻¹. Such unexpected results can be explained in that the M-g-C₃N₄-580 is rich in tri-s-triazine units (Figure 3b), which can be further protonated at a low pH to attract ABR, while triazine units in U-g-C₃N₄-580 cannot.⁴⁶ Previous studies showed that anionic dye was hardly¹⁹ adsorbed on g-C₃N₄; however, the present study gives the opposite result.

3.5. Effect of Solution Temperature on the Adsorption. Figure 12a shows adsorption isotherms of ABR on U-g-C₃N₄-580 at different adsorption temperatures. It can be seen

from Figure 11a that the adsorption capacity of U-g-C₃N₄-580 decreases with increasing adsorption temperature. Adsorption is nearly always a diffusion process with exothermic nature. High temperature can result in an increase in the mobility of the acidic compounds but can decrease the interaction of ABR with active sites of U-g-C₃N₄-580, which causes a decrease in the adsorption capacity.⁴⁶

Thermodynamic parameters such as ΔG (standard Gibbs free energy change), ΔH (standard enthalpy change), and ΔS (standard entropy change) were calculated from the following equations:⁴⁷

$$\Delta G = -RT \ln K_c \quad (6)$$

$$K_c = \frac{C_{Ae}}{C_e} \quad (7)$$

$$\ln K_c = \frac{\Delta s}{R} - \frac{\Delta H}{RT} \quad (8)$$

where T is the adsorption temperature (K), C_{Ae} and C_e are the equilibrium concentrations of ABR in g-C₃N₄ and solution (mg L⁻¹), and R is the universal gas constant (8.314 J mol⁻¹ K⁻¹). The van't Hoff plots for the adsorption of U-g-C₃N₄-580 are shown in Figure 12b, and the calculated thermodynamic parameters are given in Table 5.

The negative value of ΔG in Table 5 indicates that the adsorption is spontaneous. The increase in ΔG value with increasing adsorption temperature indicates that high temperature unfavors the adsorption. Negative ΔH values confirm that chemical bonds between ABR and U-g-C₃N₄ formed that make the adsorption exothermic; the negative ΔS values reveal decreasing chaos of the solid-solution interface during the adsorption.

3.6. Reusability and Comparison with Other Adsorbents. Reusability is an important parameter in evaluating the performance of the adsorbents. In this study, U-g-C₃N₄-580 adsorbed with ABR was separated from the solution by centrifugation and was added into 50 mL of anhydrous ethanol sonicated for 2 h, then centrifuged, washed with deionized water, and dried. Then, the regenerated U-g-C₃N₄-580 was added to the solution to adsorb ABR again, and the results are given in Figure 13, where the adsorption conditions were the same as those for pristine U-g-C₃N₄-580.

As shown in Figure 13, the adsorption ratio for ABR could still reach 80% at the fourth repeated adsorption, indicating the wonderful recyclability of U-g-C₃N₄-580.

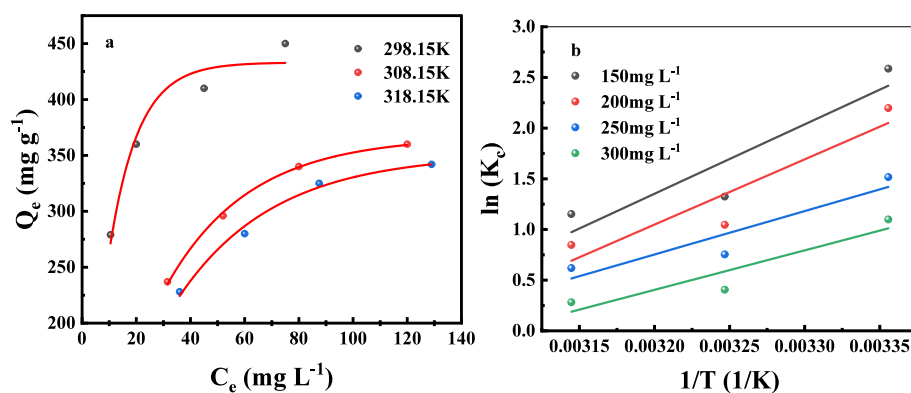


Figure 12. Adsorption isotherms (a) and Van't Hoff plots (b) of U-g-C₃N₄-580 on ARB (adsorbent dose, 100 mg; solution volume, 200 mL; initial pH of ABR solution, 1.5).

Table 5. Thermodynamic Parameters of U-g-C₃N₄-580 for ABR Adsorption

| C ₀ (mg L ⁻¹) | adsorption temperature (K) | ΔG (kJ mol ⁻¹) | ΔS (J mol ⁻¹ K ⁻¹) | ΔH (kJ mol ⁻¹) |
|--------------------------------------|----------------------------|----------------------------|---|----------------------------|
| 150 | 298.15 | -6411.94 | -170.94 | -56.94 |
| | 308.15 | -3394.42 | | |
| | 318.15 | -3048.95 | | |
| 200 | 298.15 | -5466.51 | -162.70 | -53.57 |
| | 308.15 | -2679.73 | | |
| | 318.15 | -2241.20 | | |
| 250 | 298.15 | -3758.76 | -107.70 | -35.60 |
| | 308.15 | -1931.13 | | |
| | 318.15 | -1637.42 | | |
| 300 | 298.15 | -2723.26 | -100.34 | -32.41 |
| | 308.15 | -1038.80 | | |
| | 318.15 | -745.52 | | |

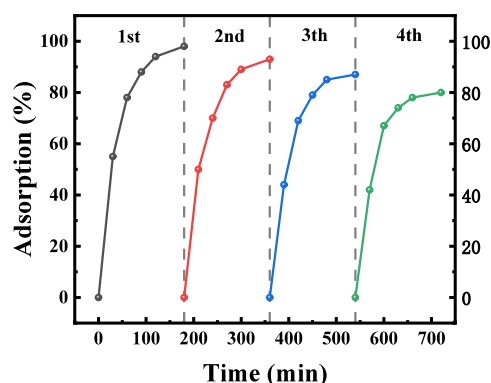


Figure 13. Readsorption properties of U-g-C₃N₄-580 after desorption with 50 mL of anhydrous ethanol (adsorbent dose, 100 mg; solution volume, 200 mL; initial pH, 1.5; initial ABR concentration for each run, 100 mg L⁻¹).

The XRD pattern and FTIR spectra of U-g-C₃N₄-580 after desorption are presented in Figure 14.

As shown in Figure 14, no peaks appeared or disappeared in both the XRD pattern and the IR spectra, indicating the excellent regeneration of U-g-C₃N₄-580. However, the XRD peak intensities of the desorbed U-g-C₃N₄-580 were much stronger than the pristine one, implying that the crystal size of U-g-C₃N₄-580 increased during the adsorption and desorption processes. Peak intensities in the range 1246–1639 cm⁻¹ enhanced after desorption demonstrate the increased relative

number of tri-s-triazine units in U-g-C₃N₄-580 during the adsorption.

In order to better understand the adsorption process, pH changes in the adsorption processes are given in Figure 15.

It can be observed from Figure 15 that, when the ABR solution pH is lower than 7.8, the solution pH increased after adsorption, indicating that adsorption proceeds via protonation of the adsorbents. However, the pH decreased in the case of higher solution pH, indicating that the U-g-C₃N₄-580 also reacts with OH⁻ in the solution.¹⁹

According to the experimental results and the related discussions, the protonation mechanism of g-C₃N₄ for ABR is proposed in Figure 16. It can be observed from Figure 16 that g-C₃N₄ is protonated in acidic solution where the ABR is in the form R-SO₃⁻, and the ABR is adsorbed by the protonated g-C₃N₄ due to electrostatic attraction. Usually, the bonding amino groups are the most easily protonated followed by the nitrogen in the tri-s-triazine units.²⁹ Triazine units are hardly protonated in the solution.^{46,48} The adsorption capacity of U-g-C₃N₄-580 is higher than that of M-g-C₃N₄-580 at a pH higher than 2.0 because it possesses a larger surface area. However, as M-g-C₃N₄-580 contains more tri-s-triazine units than U-g-C₃N₄-580, M-g-C₃N₄-580 has much larger adsorption capacity at an initial pH of 1.0.⁴⁸ Both ABR and g-C₃N₄ contained aromatic moieties in the structure, and π-π stacking can contribute to the adsorption. Moreover, g-C₃N₄ contains sec-((R)₂-NH) groups; hydrogen bonds can be formed between the hydrogen atoms therein and the oxygen atoms in ABR.⁴²

The maximum adsorption capacity of g-C₃N₄ prepared in this work and those of other adsorbents for ARB are shown in Table 6.

As Table 6 shows, the maximum adsorption capacity of M-g-C₃N₄-580 can reach 25635.64 mg/g at ambient temperature, which is 100 times higher than those of other adsorbents, indicating its superiority in the adsorption field. As the price of the precursor (melamine, ca. \$1.00 per kg in the present Chinese market) for preparing M-g-C₃N₄-580 is very low, the application of M-g-C₃N₄-580 in acid dye wastewater treatment would be greatly expected.

4. CONCLUSIONS

In this study, we report that g-C₃N₄ synthesized by direct calcination of urea and melamine was highly efficient for the adsorption of the ABR dye from aqueous solution. The optimum calcination temperature for preparing both materials

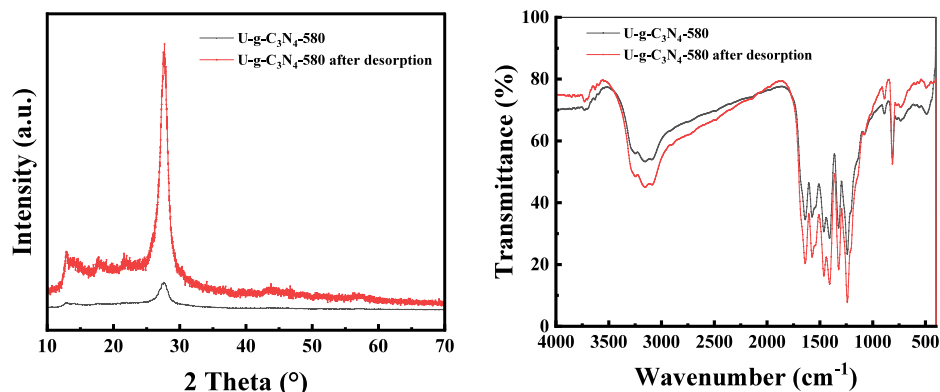


Figure 14. XRD pattern (left) and FTIR spectra (right) of U-g-C₃N₄-580 after desorption with 50 mL of anhydrous ethanol (adsorbent dose, 100 mg; solution volume, 200 mL; initial pH of ABR solution, 1.5; adsorption temperature, 298.15 K; initial ABR concentration, 200 mg L⁻¹).

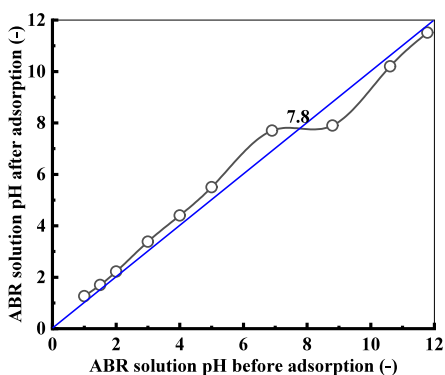


Figure 15. Change in ABR solution pH during the adsorption by U-g-C₃N₄-580 (adsorbent dose, 15 mg; initial ABR concentration, 800 mg L⁻¹; solution volume, 200 mL; adsorption temperature, 25 °C).

was 580 °C, where the specific surface area of g-C₃N₄ obtained from urea (U-g-C₃N₄) was 2.74 times that from melamine (M-g-C₃N₄). The adsorption capacity strongly increases with

Table 6. Comparison of the Maximum Adsorption Capacity of Various Adsorbents for ABR

| adsorbents | T (°C) | Q _m (mg/g) | reference |
|--|--------|-----------------------|-----------|
| AC from corn straw prepared by microwave | 45 | 178.57 | 14 |
| U-g-C ₃ N ₄ -580 | 25 | 2063.04 | this work |
| M-g-C ₃ N ₄ -580 | 25 | 25635.64 | this work |
| NiO(111) nanosheets | 25 | 30.4 | 13 |

decreasing initial solution pH and adsorption temperature. U-g-C₃N₄ had a superior adsorption effect to that of M-g-C₃N₄ at pH > 2.0. However, M-g-C₃N₄ has a much higher adsorption performance at an initial pH of 1.0, where the maximum adsorption capacity can reach 25 635.64 mg g⁻¹, which was 100 times higher than that of other competitive adsorbents reported to date. The pseudo-second-order kinetic model and Langmuir isotherm model can best fit the adsorption data. The adsorption is spontaneous and exothermic. Electrostatic interaction between the protonated g-C₃N₄ and ABR

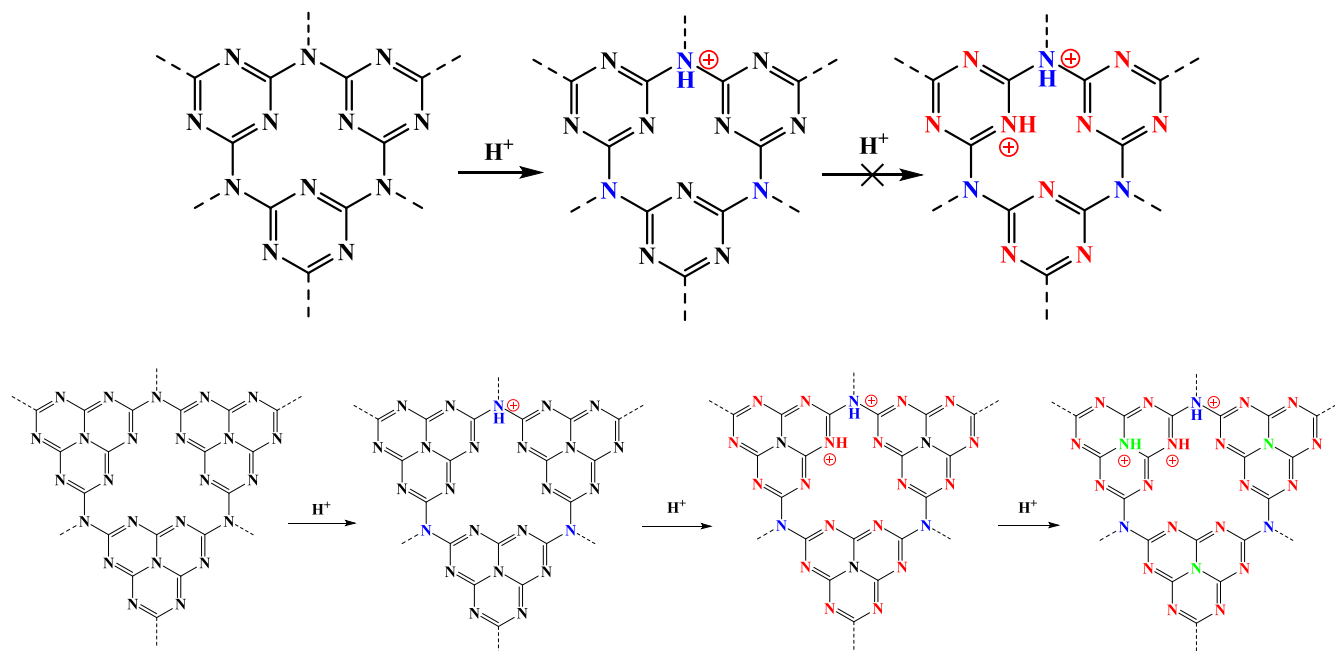


Figure 16. Possible protonation mechanism for ABR on g-C₃N₄.

predominates the adsorption. $g\text{-C}_3\text{N}_4$ can be easily regenerated by ethanol, and the regenerated $g\text{-C}_3\text{N}_4$ can be successfully used for the new adsorption cycle, showing its strong applicability in dye wastewater treatment.

AUTHOR INFORMATION

Corresponding Author

Yongjun Liu – College of Environmental Science and Engineering, Dalian Maritime University, Dalian 116026, People's Republic of China; orcid.org/0000-0001-5802-9701; Phone: 86-411-84725275; Email: lyjglow@dlnu.edu.cn; Fax: 86-411-84727670

Author

Huiwen Sun – College of Environmental Science and Engineering, Dalian Maritime University, Dalian 116026, People's Republic of China

Complete contact information is available at:

<https://pubs.acs.org/10.1021/acsomega.4c02705>

Notes

The authors declare no competing financial interest.

ACKNOWLEDGMENTS

This work was supported by the National Natural Science Foundation of China (11005014, 11675031).

REFERENCES

- (1) Maheshwari, K.; Agrawal, M.; Gupta, A. B. Dye pollution in water and wastewater. *Novel Materials for Dye-containing Wastewater Treatment*; Springer: Singapore 2021, 1–25.
- (2) Yaseen, D. A.; Scholz, M. Textile dye wastewater characteristics and constituents of synthetic effluents: a critical review. *International Journal of Environmental Science and Technology* 2019, 16, 1193–1226.
- (3) Sun, D.; Zhang, X.; Wu, Y.; et al. Adsorption of anionic dyes from aqueous solution on fly ash. *Journal of Hazardous Materials* 2010, 181 (1), 335–342.
- (4) Solayman, H. M.; Hossen, M. A.; Abd Aziz, A.; et al. Performance evaluation of dye wastewater treatment technologies: A review. *Journal of Environmental Chemical Engineering* 2023, 11, 109610.
- (5) Luo, Y.; Wei, X.; Gao, B.; et al. Synergistic adsorption-photocatalysis processes of graphitic carbon nitrate ($g\text{-C}_3\text{N}_4$) for contaminant removal: kinetics, models, and mechanisms. *Chemical Engineering Journal* 2019, 375, 122019.
- (6) Cui, Z.; Yang, H.; Zhao, X. Enhanced photocatalytic performance of $g\text{-C}_3\text{N}_4/\text{Bi}_4\text{Ti}_3\text{O}_{12}$ heterojunction nanocomposites. *Materials Science and Engineering: B* 2018, 229, 160–172.
- (7) Wang, X.; Deng, B.; Yu, L.; et al. Degradation of azo dyes Congo red by MnBi alloy powders: performance, kinetics and mechanism. *Mater. Chem. Phys.* 2020, 251, 123096.
- (8) Kishor, R.; Purchase, D.; Saratale, G. D.; et al. Ecotoxicological and health concerns of persistent coloring pollutants of textile industry wastewater and treatment approaches for environmental safety. *J. Environ. Chem. Eng.* 2021, 9, 105012.
- (9) Gómez, V.; Larrechi, M. S.; Callao, M. P. Kinetic and adsorption study of acid dye removal using activated carbon. *Chemosphere* 2007, 69 (7), 1151–1158.
- (10) Ayati, A.; Shahrak, M. N.; Tanhaei, B.; et al. Emerging adsorptive removal of azo dye by metal–organic frameworks. *Chemosphere* 2016, 160, 30–44.
- (11) Bingöl, D.; Veli, S.; Zor, S.; et al. Analysis of adsorption of reactive azo dye onto CuCl_2 doped polyaniline using Box–Behnken design approach. *Synth. Met.* 2012, 162 (17–18), 1566–1571.
- (12) Muedas-Taípe, G.; Maza Mejía, I. M.; Santillan, F. A.; et al. Removal of azo dyes in aqueous solutions using magnetized and chemically modified chitosan beads. *Mater. Chem. Phys.* 2020, 256, 123595.
- (13) Song, Z.; Chen, L.; Hu, J.; et al. NiO (111) nanosheets as efficient and recyclable adsorbents for dye pollutant removal from wastewater. *Nanotechnology* 2009, 20 (27), 275707.
- (14) Ren, X.; Wang, S.; Jin, Y.; et al. Adsorption properties of reactive dyes on the activated carbon from corn straw prepared by microwave pyrolysis. *Desalination and Water Treatment* 2020, 200, 296–303.
- (15) Luo, Y.; Zhu, Y.; Han, Y.; et al. $g\text{-C}_3\text{N}_4$ -based photocatalysts for organic pollutant removal: a critical review. *Carbon Research.* 2023, 2 (1), 14.
- (16) Pawar, R. C.; Son, Y.; Kim, J.; et al. Integration of ZnO with $g\text{-C}_3\text{N}_4$ structures in core-shell approach via sintering process for rapid detoxification of water under visible irradiation. *Curr. Appl. Phys.* 2016, 16 (1), 101.
- (17) Wang, X.; Maeda, K.; Thomas, A.; et al. A metal-free polymeric photocatalyst for hydrogen production from water under visible light. *Nat. Mater.* 2009, 8 (1), 76–80.
- (18) Xu, H. Y.; Wu, L. C.; Zhao, H.; et al. Synergistic effect between adsorption and photocatalysis of metal-free $g\text{-C}_3\text{N}_4$ derived from different precursors. *PLoS one* 2015, 10 (11), No. e0142616.
- (19) Zhu, B.; Xia, P.; Ho, W.; et al. Isoelectric point and adsorption activity of porous $g\text{-C}_3\text{N}_4$. *Appl. Surf. Sci.* 2015, 344, 188–195.
- (20) Stefa, S.; Griniezaki, M.; Dimitropoulos, M.; et al. Highly porous thin-layer $g\text{-C}_3\text{N}_4$ nanosheets with enhanced adsorption capacity. *ACS Applied Nano Materials* 2023, 6 (3), 1732–1743.
- (21) Zhang, L.; Li, L.; Sun, X.; et al. ZnO-layered double hydroxide/graphitic carbon nitride composite for consecutive adsorption and photodegradation of dyes under UV and visible lights. *Materials* 2016, 9 (11), 927.
- (22) Zhao, L.; Lv, W.; Hou, J.; et al. Synthesis of magnetically recyclable $g\text{-C}_3\text{N}_4/\text{Fe}_3\text{O}_4/\text{ZIF-8}$ nanocomposites for excellent adsorption of malachite green. *Microchemical Journal* 2020, 152, 104425.
- (23) Wang, J.; Wang, C.; Shi, A. An innovative approach for landfill leachate treatment based on selective adsorption of humic acids with carbon nitride. *Chemical Engineering Journal* 2023, 461, 142090.
- (24) Pham, T.-T.; Shin, E. W. Influence of $g\text{-C}_3\text{N}_4$ precursors in $g\text{-C}_3\text{N}_4/\text{NiTiO}_3$ composites on photocatalytic behavior and the interconnection between $g\text{-C}_3\text{N}_4$ and NiTiO_3 . *Langmuir* 2018, 34 (44), 13144–13154.
- (25) El Messaoudi, N.; Ciğeröglü, Z.; Şenol, Z. M.; et al. A comparative review of the adsorption and photocatalytic degradation of tetracycline in aquatic environment by $g\text{-C}_3\text{N}_4$ -based materials. *Journal of Water Process Engineering* 2023, 55, 104150.
- (26) Fronczak, M. Adsorption performance of graphitic carbon nitride-based materials: current state of the art. *Journal of Environmental Chemical Engineering* 2020, 8 (5), 104411.
- (27) GB/T 21888-2023; C.I. Acid red131 (Acid brilliant red P-9B 150%); Chinese standard.
- (28) Yang, W.; Jia, L.; Wu, P.; et al. Effect of thermal program on structure–activity relationship of $g\text{-C}_3\text{N}_4$ prepared by urea pyrolysis and its application for controllable production of $g\text{-C}_3\text{N}_4$. *J. Solid State Chem.* 2021, 304, 122545.
- (29) Wang, L.; Chen, D.; Miao, S.; et al. Nitric acid-assisted growth of InVO_4 nanobelts on protonated ultrathin C_3N_4 nanosheets as an S-scheme photocatalyst with tunable oxygen vacancies for boosting CO_2 conversion. *Chemical Engineering Journal* 2022, 434, 133867.
- (30) Raaja Rajeshwari, M.; Kokilavani, S.; Sudheer Khan, S. Recent developments in architecturing the $g\text{-C}_3\text{N}_4$ based nanostructured photocatalysts: synthesis, modifications and applications in water treatment. *Chemosphere* 2022, 291, 132735.
- (31) Yang, H.-C.; Chao, M.-W.; Chou, C.-J.; et al. Mushroom waste-derived $g\text{-C}_3\text{N}_4$ for methyl blue adsorption and cytotoxic test for Chinese hamster ovary cells. *Mater. Chem. Phys.* 2020, 244, 122715.
- (32) Li, J.; Xiong, Y.; Wan, H.; et al. In-situ investigation of dye pollutant adsorption performance on graphitic carbon nitride surface: atr spectroscopy experiment and md simulation insight. *Journal of Hazardous Materials* 2021, 418, 126297.

- (33) Ren, B.; Xu, Y.; Zhang, L.; et al. Carbon-doped graphitic carbon nitride as environment-benign adsorbent for methylene blue adsorption: kinetics, isotherm and thermodynamics study. *Journal of the Taiwan Institute of Chemical Engineers* **2018**, *88*, 114–120.
- (34) Wang, Z.; Chen, L.; Du, X.; et al. A “pillared” process to construct graphitic carbon nitride based functionalized mesoporous materials. *RSC Adv.* **2016**, *6* (19), 15605–15609.
- (35) Yan, T.; Chen, H.; Wang, X.; et al. Adsorption of perfluorooctane sulfonate (pfos) on mesoporous carbon nitride. *RSC Adv.* **2013**, *3* (44), 22480.
- (36) Cığeroğlu, Z.; Kazan-Kaya, E. S.; El Messaoudi, N.; et al. Remediation of tetracycline from aqueous solution through adsorption on *g*-C₃N₄-ZnO-BaTiO₃ nanocomposite: optimization, modeling, and theoretical calculation. *J. Mol. Liq.* **2023**, *369*, 120866.
- (37) Xiong, S.; Liu, X.; Zhu, X.; et al. One-step preparation of well-dispersed spindle-like Fe₂O₃ nanoparticles on *g*-C₃N₄ as highly efficient photocatalysts. *Ecotoxicology and Environmental Safety* **2021**, *208*, 111519.
- (38) Wang, F.; Tang, T.; Zhang, R.; et al. Magnetically recyclable cos-modified graphitic carbon nitride-based materials for efficient immobilization of gaseous elemental mercury. *Fuel* **2022**, *326*, 125117.
- (39) Ren, B.; Xu, Y.; Zhang, L.; et al. Carbon-doped graphitic carbon nitride as environment-benign adsorbent for methylene blue adsorption: kinetics, isotherm and thermodynamics study. *Journal of the Taiwan Institute of Chemical Engineers* **2018**, *88*, 114–120.
- (40) Haque, E.; Jun, J. W.; Talapaneni, S. N.; et al. Superior adsorption capacity of mesoporous carbon nitride with basic CN framework for phenol. *J. Mater. Chem.* **2010**, *20* (48), 10801.
- (41) Lafi, R.; Montasser, I.; Hafiane, A. Adsorption of congo red dye from aqueous solutions by prepared activated carbon with oxygen-containing functional groups and its regeneration. *Adsorption Science & Technology* **2019**, *37* (1–2), 160–181.
- (42) Konicki, W.; Aleksandrak, M.; Moszyński, D.; et al. Adsorption of anionic azo-dyes from aqueous solutions onto graphene oxide: equilibrium, kinetic and thermodynamic studies. *J. Colloid Interface Sci.* **2017**, *496*, 188–200.
- (43) Maneerung, T.; Liew, J.; Dai, Y.; et al. Activated carbon derived from carbon residue from biomass gasification and its application for dye adsorption: kinetics, isotherms and thermodynamic studies. *Bioresour. Technol.* **2016**, *200*, 350–359.
- (44) Lütke, S. F.; Igansi, A. V.; Pegoraro, L.; et al. Preparation of activated carbon from black wattle bark waste and its application for phenol adsorption. *Journal of Environmental Chemical Engineering* **2019**, *7* (5), 103396.
- (45) Anbia, M.; Haqshenas, M. Adsorption studies of Pb(II) and Cu(II) ions on mesoporous carbon nitride functionalized with melamine-based dendrimer amine. *International Journal of Environmental Science and Technology* **2015**, *12* (8), 2649–2664.
- (46) Rehnelt, K. Über Salze des 2, 4, 6-Triamino-triazins-(1, 3, 5) [Melamins]. *Monatshefte für Chemie und verwandte Teile anderer Wissenschaften* **1953**, *84*, 257–262.
- (47) Qu, W.; Yuan, T.; Yin, G.; et al. Effect of properties of activated carbon on malachite green adsorption. *Fuel* **2019**, *249*, 45–53.
- (48) Bann, B.; Miller, S. A. Melamine and derivatives of melamine. *Chem. Rev.* **1958**, *58* (1), 131–72.